Journal of Materials Chemistry A

PAPER

View Article Online
View Journal | View Issue

Cite this: J. Mater. Chem. A, 2014, 2, 17944

Nanocavity-engineered Si/multi-functional carbon nanofiber composite anodes with exceptional high-rate capacities†

Zheng-Long Xu, Biao Zhang, Sara Abouali, Mohammad Akbari Garakani, Jiaqiang Huang, Jian-Qiu Huang, Elham Kamali Heidari and Jang-Kyo Kim*

Received 17th August 2014
Accepted 2nd September 2014

DOI: 10.1039/c4ta04257c

www.rsc.org/MaterialsA

A facile and scalable electrospinning method is employed to fabricate *in situ* N-doped, porous graphitic carbon nanofibers (CNFs) containing Si nanoparticles surrounded by nanocavities as durable high-rate Li-ion anodes. Nanocavities are created within the graphitic carbon spheres by electroless etching of the Si nanoparticles, which function not only as buffer to accommodate the volumetric expansion of Si upon lithiation but also as a conducting network for fast electron/ion transport. The Fe_3C catalyst simultaneously formed within the fiber promotes the formation of highly graphitic carbon structures while the nitric acid etchant *in situ* generates functional CNFs with numerous mesopores and oxygenated functional groups, offering extra reaction sites for Li ions. With the ameliorating structural features acting synergistically, the resultant C–Si/F–CNF electrode delivers an exceptional initial reversible capacity of 1548 mA h g^{-1} at 0.1 A g^{-1}, and remarkable high-rate capacities of 770 and 580 mA h g^{-1} at 2.0 and 5.0 A g^{-1} after 70 cycles with excellent capacity retention.

1. Introduction

Lithium ion batteries (LIBs) possessing high energy densities, high rate capabilities and long cyclic life have been considered one of the most promising portable energy storage devices to satisfy the increasingly demanding applications, such as electric vehicles, smart grids and communication devices.[1,2] The low specific capacity of commercial graphite, *i.e.* 370 mA h g^{-1}, has attracted significant research to identify alternative anodes with higher energy densities, low costs and improved safety.[3] Among many potential electrode materials known to us, Si has the highest theoretical capacity of ~4200 mA h g^{-1} apart from other advantages, such as a low working potential of ~370 mV, nontoxicity and abundance in nature.[4] However, during the charge and discharge processes, the inherently insulating Si suffers from 300% volumetric changes that not only cause electrode pulverization and loss of electrical contact with the current collector, but also lead to the formation of insulating solid electrolyte interphase (SEI) layers at the expense of the electrolyte. To prolong the cyclic life and achieve high rate capabilities of Si-based anodes, much research effort is needed to improve the ion/electron transport and the structural integrity of Si.[5–7]

One of the most attractive strategies to mitigate the above challenges is to employ the electrospinning technique to *in situ* encapsulate Si particles within a carbon nanofiber (CNF) matrix. There are many advantages arising from the use of such 1D CNF composite electrodes containing active metals or metal oxide particles.[8–10] They include the following: (i) the electrospinning technique is facile, versatile and capable of one-pot synthesis of multi-phase composite fibers; (ii) the electrospun flexible and freestanding composite thin films can be directly employed as electrodes without any binders or additives after carbonization, which can be scaled up at low manufacturing costs for large-scale applications; (iii) the hierarchical pore structured and self-supported interconnected CNF matrix with a large surface area provides electron transport paths and allows the infiltration of the electrolyte to reach embedded, individual active particles; and (iv) the soft carbon matrix functions as a buffer to relieve the stress resulting from the volume expansion of the active particles during the Li ion intercalation/extraction process. Diverse Si/CNF composites with different structures have been developed with different degrees of success in improving the electrochemical performance, such as Si/CNF,[10–13] Si/CNF core–shell,[14–16] Si/porous CNF,[17,18] Si/carbon nanotube (CNT)/CNF[19] and Si/graphene (G)/CNF.[20–22] Even with the improved structure and electrochemical performance, there still exist several important issues that need to be addressed: namely, (i) the moderate electrical conductivities of CNFs prepared from carbonized polymers, like polyvinyl alcohol (PVA) or polyacrylonitrile (PAN), are the major bottleneck in achieving fast Li ion transfer and much enhanced high-rate capabilities; (ii)

Department of Mechanical and Aerospace Engineering, The Hong Kong University of Science and Technology, Clear Water Bay, Kowloon, Hong Kong. E-mail: mejkkim@ust.hk; Fax: +852 2358 1543; Tel: +852-2358-7207

† Electronic supplementary information (ESI) available. See DOI: 10.1039/c4ta04257c

there is a limit in providing sufficient Li ion storage sites by the solid CNF matrix even with *in situ* created pores;[10–13] and (iii) the solid CNF matrix with little void space surrounding the Si particles has limited potential to relieve the stress due to drastic volume expansion, causing the Si particles to be cracked and disintegrated.[23]

It has been demonstrated that nitrogen doping (N-doping) of CNFs or CNTs may not only enhance the electrical conductivities of carbon materials, but also can improve the Li ion storage capacities *via* the creation of defect sites.[24–26] Moreover, extra void spaces were engineered around the Si particles using different morphological strategies, like Si core/carbon hollow shell,[27,28] Si/carbon yolk–shell[29] and Si/C pomegranate-shaped structures,[30] to achieve improved cyclic stability. Although remarkable improvements were made with these novel structures, the contacts between the Si particles and the carbon were mainly through a point-to-point mode which may limit the improvement of Li ion and electron transport.[23,31]

Herein, we developed freestanding, *in situ* N-doped graphitic and porous CNFs containing engineered nanocavities to surround the Si particles (C–Si/F–CNF) using the one-pot electrospinning method. In addition to the nanocavity-engineered Si nanoparticles, mesopores and oxygenated functional groups were simultaneously created by sequential etching of the electrospun CNF composites using hydrofluoric acid and fuming nitric acid. The resulting novel structure, schematically shown in Fig. 1, possesses several unique features and capabilities that the other structural forms lack. The nanocavity-engineered composite electrodes delivered excellent electrochemical performance with a combination of exceptional high initial reversible capacities and excellent high-rate capacities along with remarkable cyclic stability.

2. Experimental

2.1 Fabrication of nanocavity-engineered Si particle/functionalized CNF (C–Si/F–CNF) composites

The precursor materials and the machine used for electrospinning were essentially the same as those reported previously.[9,12] 0.5 g polyacrylonitrile (PAN, $M_w = 150\,000$ supplied by Aldrich) was magnetically stirred in 14 ml dimethylformamide (DMF, by Aldrich) for 8 h to form homogenous solution, then 0.1 g well-dispersed Si particles (average size 50–100 nm, supplied by Shanghai ST-Nano Science & Technology Co.) and 0.1 g iron(III) acetylacetonate (by Aldrich) were sequentially added to the PAN solution and stirred overnight. The mixture was electrospun into fibers on a single-nozzle electrospinning unit (KATO Tech. Co., Japan) at a high voltage of 18 kV and a constant flow rate of 1 ml h^{-1}. The distance between the 19G needle and the rotating collector was fixed at 15 cm. After peeling off from the collector, the composite film was stabilized at 220 °C for 3 h in air and carbonized at 750 °C for 1 h in N_2, which was designated as Si/Fe/CNF. The Si/Fe/CNF composite films were immersed in HF solution (5 wt%) for 30 min to partially etch the Si particles with the assistance of Fe_3C. The etched composite films were further treated in fuming HNO_3 solution (68 wt%) to remove the residual Fe_3C and simultaneously functionalize the CNF matrix with oxygen-containing functional groups. After washing with de-ionized water, the resultant composites were designated as C–Si/F–CNF. For comparison, Si/CNF films were also prepared in the same way without iron(III) acetylacetonate.

2.2 Characterization and electrochemical tests

The morphologies of the as-prepared materials were examined on a scanning electron microscope (SEM, JEOL 6700F) and a transmission electron microscope (TEM, JEOL 2010 and 2010F). The surface elements were analysed using an X-ray photoelectron spectroscopy system (XPS, PHI5600, Physical Electronics), powder X-ray diffraction analysis (XRD, Philips, PW 1830) was used to evaluate the phase structures between $2\theta = 10°$ and 90° at a scan rate 2° min^{-1}. The nitrogen adsorption and desorption isotherms were studied at 77 K on a Micromeritics ASAP 2020 analyzer and the corresponding surface areas were determined using the Brunauer–Emmett–Teller (BET) method. The electric conductivities of the various Si/CNF composites were measured on a four-probe resistivity/Hall system (HL5500PC, Bio-Rad). The compositions of the composite films were determined by thermogravimetry analysis (TGA, Q5000) at a heating rate 10 °C min^{-1} in air.

The films were cut into 10 × 10 mm^2 squares which were directly assembled into 2032 type coin cells inside an argon-filled glove box using lithium foil as the counter electrode. 1 M $LiPF_6$ in a solution of ethyl carbonate (EC) : dimethyl carbonate (DMC) mixture (1 : 1 v/v) was used as the electrolyte and microporous polyethylene films (Celgard 2400) were used as the separator. The electrochemical tests were carried out between 0 and 3.0 V at different current densities on a LAND 2001 CT battery tester. The cyclic voltammetry (CV) test was performed on a CHI600c electrochemical workstation at a scan rate 0.1 mV s^{-1}. The electrochemical impedance spectra (EIS) were obtained at a

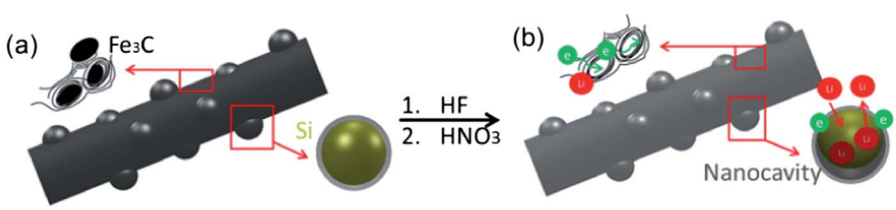

Fig. 1 Schematics of (a) Si/Fe/CNF and (b) C–Si/F–CNF composites: etching of the Si/Fe/CNF composite by HF and HNO_3 to form nanocavities around Si particles within the carbon sheath, and *in situ* creation of functional groups and graphitic pores in the CNF matrix.

constant perturbation amplitude of 5 mV in the frequency range between 100 kHz and 10 mHz.

3. Results and discussion

The *in situ* N-doped porous graphitic CNFs containing Si particles with surrounding nanocavities were prepared by a two-step process, namely (i) one-pot electrospinning of Si/Fe/CNF freestanding films, followed by (ii) creation of nanocavities using HF and functionalization by HNO_3 to form C–Si/F–CNF, as schematically illustrated in Fig. 1. The corresponding overall morphologies are shown in Fig. S1:† both the Si/Fe/CNF and C–Si/F–CNF composites consisted of smooth fibrous structures of 100–300 nm in diameter with embedded Si individual particles or clusters. Typical TEM images of Si/Fe/CNF (Fig. S2†) indicate that the CNF matrix enclosing the Si particles was highly graphitic.[28] The small particles are Fe_3C as confirmed by the SAED pattern (see the inset in Fig. S2†). The graphitic carbon spheres not only ameliorated the electron/ion transport due to the enhanced electrical conductivity and the porous structure, but also acted as Li ion storage sites.[24–26] The mesopores of 5–15 nm in diameter present around the Fe_3C particles (Fig. S2†) were probably a trace of progressive growth of graphitization catalyzed by the Fe_3C particles during the thermal treatment.[32] After the chemical treatment, Si particles were partially etched to create nanoscale cavities of ~20 nm in size (Fig. 2a and c) within the graphitic carbon sheath of 5–10 nm in thickness (Fig. 2c). The nanocavity size can be tuned by controlling the etching time, as shown in Fig. S3.† An optimized cavity size and residual Si particles were obtained after etching for about 30 min.[27,34]

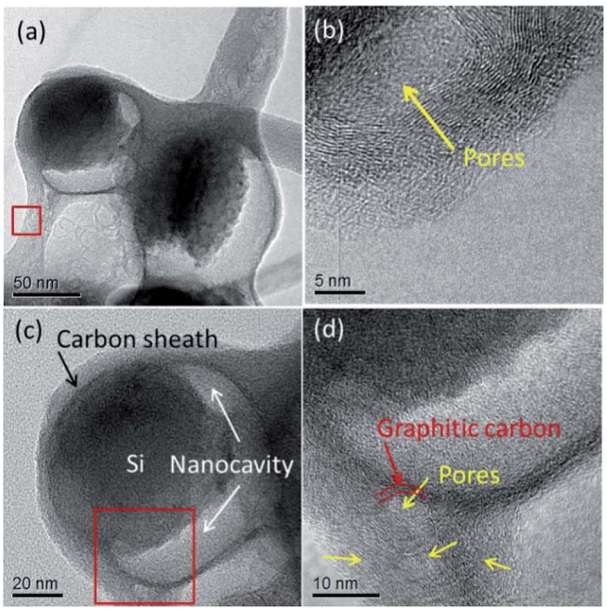

Fig. 2 (a) TEM image of C–Si/F–CNF, (b–d) HRTEM images of (a); (b and d) magnified views of squares in (a) and (c), respectively.

Actually, the Si particles in Fig. 2c maintained intimate contacts with the surrounding carbon sheaths, and such a face-to-face contact mode allowed excellent electronic conduction through the interconnected networks.[31] The electroless chemical reactions involved in the etching process with HF and Fe_3C are given:[31,33,34]

$$Si + Fe^{3+} + 3HF + 3HF_2^- \rightarrow H_2SiF_6 + 2H^+ + H_2 + 3F^- + e^- + Fe^{2+} \quad (1)$$

$$H^+ + e^- \rightarrow 1/2H_2 \quad (2)$$

Additional nanoscale pores surrounded by graphitic carbon layers were created within the CNF matrix after the removal of residual Fe_3C particles by HNO_3 (Fig. 2b and d). As a result, both the pore volume and the surface area significantly increased (see Table 1).

The XRD patterns shown in Fig. 3a confirmed the above findings, signifying the presence of Fe_3C (PDF card: 89-2867) and graphitic carbon in the Si/Fe/CNF composite, as well as the Si particles (PDF card: 27-1402) without any Fe_3C residue in the C–Si/F–CNF composite.[20,25] The nitrogen adsorption and desorption curves (Fig. 3b) show that the C–Si/F–CNF composite contained significantly more pores of size peaked at ~3 nm than the Si/Fe/CNF composite, consistent with the above TEM results. The corresponding specific BET surface area of the former composite was much larger than the latter (*i.e.* 224.1 *vs.* 90.5 $m^2\ g^{-1}$, see Table 1). To clearly identify the nanocavities created by partially etching the Si particles, the BJH pore size distribution is plotted between 10 and 60 nm, as shown in Fig. S4.† C–Si/F–CNF exhibited much increased pore volumes between 15 and 30 nm, similar to the previous observation.[31]

The Raman spectra (Fig. 3c) present sharp peaks at 521 cm^{-1} for both the composites, which correspond to the Si particles.[35] The peaks centred at about 1350, 1580 and 2700 cm^{-1} are attributed to the D band originating from disordered carbon, the G band representing ordered carbon and the 2D band corresponding to the graphene-like carbon, respectively.[36] It is worth

Table 1 XPS elemental compositions (at.%), Raman spectral I_D/I_G intensity ratio, BET surface areas, pore volumes and electrical conductivities of Si/Fe/CNF and C–Si/F–CNF composites

	Elemental compositions (at.%)								
Samples	C	Si	Fe	N	O	I_D/I_G	BET $m^2\ g^{-1}$	Pore volume $cm^3\ g^{-1}$	Conductivity S cm^{-1}
Si/Fe/CNF	86.16	2.22	0.70	4.62	6.29	0.56	90.5	0.2659	1.31
C–Si/F–CNF	78.47	2.80	0.02	4.72	13.89	1.68	224.1	0.6158	2.1×10^{-2}

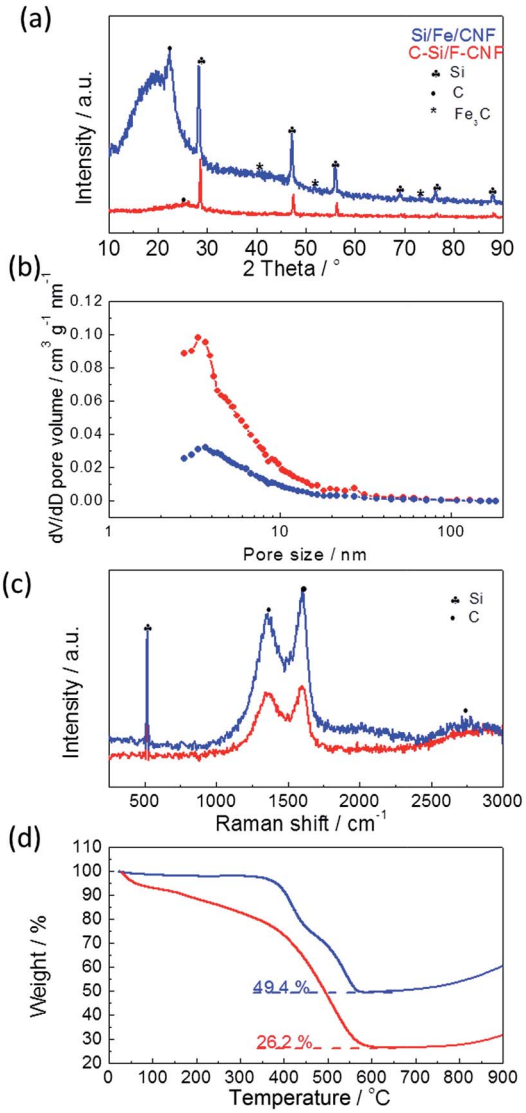

Fig. 3 (a) XRD patterns; (b) pore size distributions; (c) Raman spectra and (d) TGA curves of Si/Fe/CNF and C–Si/F–CNF composites.

noting that the much stronger D to G band intensity ratio, I_D/I_G, for C–Si/F–CNF than for Si/Fe/CNF (see Table 1) should stem from the etching and functionalization processes using the strong acids. The TGA result (Fig. 3d) presents a gradual weight reduction of the C–Si/F–CNF composite between 30 and 400 °C due to the decomposition of oxygen functional groups and the oxidization of CNFs, reaching 26.2 wt% at 600 °C representing only the Si particles. In contrast, the curve of the Si/Fe/CNF composite was flat until ~320 °C, which was followed by a sudden weight drop till 580 °C where both CNF and Fe_3C oxidized,[25] as confirmed by the DTA analysis (see Fig. S5†).

Representative XPS spectra are shown in Fig. 4. Unlike the C1s spectrum of Si/Fe/CNF, the C–Si/F–CNF composite presented a much stronger peak at 288 eV (C=O) in Fig. 4a, indicating successful oxygenation by HNO_3, as confirmed by the increased O1s content from 6.29 to 13.89 at.% (Table 1). This

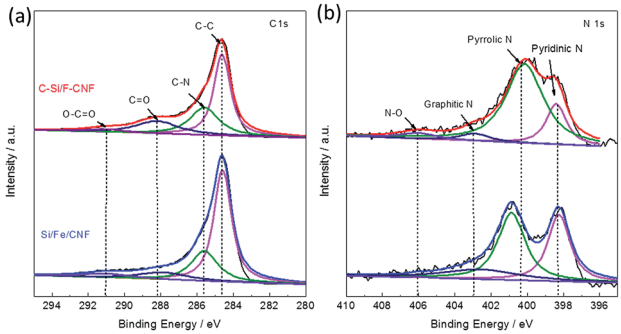

Fig. 4 Deconvoluted C1s (a) and N1s (b) XPS spectra of Si/Fe/CNF and C–Si/F–CNF composites, respectively.

functional group was responsible for the enhancement of Li ion storage capacity by faradic reactions:[24,25]

$$Li^+ + C{=}O + e^- \leftrightarrow C{-}OLi \quad (3)$$

The PAN precursor with an inherently high N-content (~26.4 wt%) is believed to be the main source of the N-doped CNFs.[25,26] The N1s spectra in Fig. 4b present three broad peaks centred at 398.5 eV, 400.2 eV and 403.2 eV, corresponding to pyridinic-N, pyrrolic-N and graphitic-N, respectively.[37] The carbonization temperature was one of the most critical factors influencing the remnant N-content in CNFs.[37] The marginal down-shift of the pyrrolic-N peak in the C–Si/F–CNF composite is attributed to a coordinated binding energy effect.[38] The N–O and pyrrolic-N contents increased due to the oxidization of CNFs after the acid treatment, consistent with the XPS result of C1s (Fig. 4a).

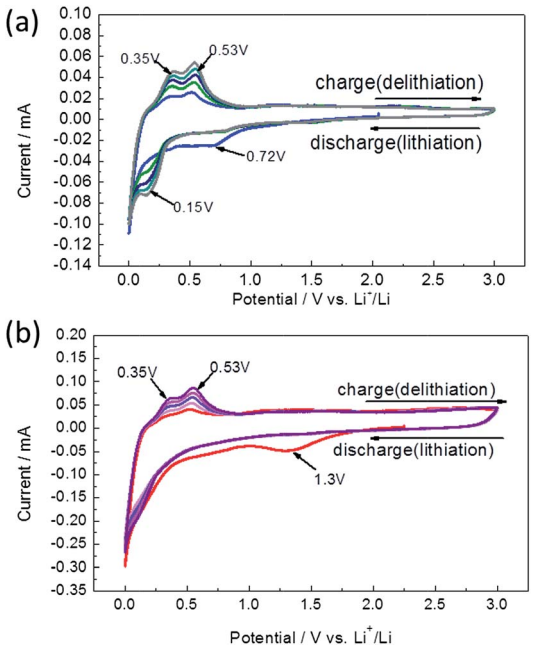

Fig. 5 CV curves of (a) Si/Fe/CNF and (b) C–Si/F–CNF composite electrodes.

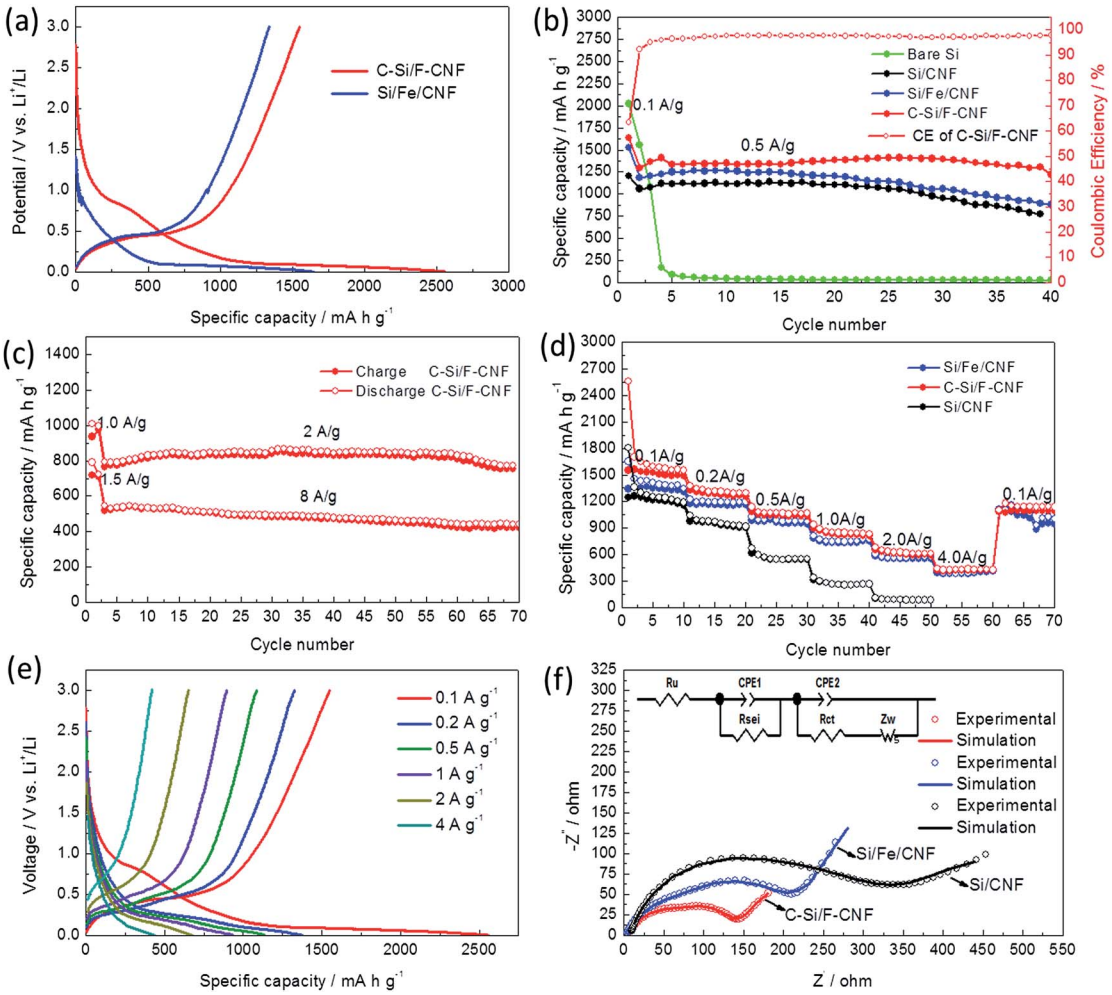

Fig. 6 (a) Charge/discharge profiles of Si/Fe/CNF and C–Si/F–CNF electrodes in the first cycle at 0.1 A g^{-1}; (b) cyclic performance and coulombic efficiency of the C–Si/F–CNF electrode compared with other electrodes measured at 0.5 A g^{-1}; (c) high-rate capacities of the C–Si/F–CNF electrode at 2 and 8 A g^{-1} for 70 cycles; (d) rate performance of Si/CNF, Si/Fe/CNF and C–Si/F–CNF electrodes at current densities ranging from 0.1 to 4.0 A g^{-1}; (e) charge/discharge profiles of C–Si/F–CNF at different current densities; (f) Nyquist plots and *Z*-view simulation of three different electrodes after the rate tests in Fig. 6(d).

Meanwhile, the pyridinic-N content remained relatively high, which in turn contributed to large vacant sites to store Li ions for enhanced electrochemical capacities.[37]

With the above unique structural features and ameliorating functional groups, the C–Si/F–CNF composite electrode presented excellent electrochemical behavior, as shown in Fig. 5 and 6. The cyclic voltammetry (CV) curves of the Si/Fe/CNF and C–Si/F–CNF electrodes (Fig. 5) showed similar characteristic peaks at 0.72 and 1.3 V in the first cathodic sweep, corresponding to the formation of SEI layers and electrolyte consumption, respectively. The sharp peaks appeared below 0.2 V corresponding to lithiation of Si materials according to the reaction:

$$\text{c-Si} + x\text{Li}^+ + x\text{e}^- \rightarrow \text{Li}_x\text{Si} \quad (4)$$

It is noted that the inset SAED pattern (see Fig. 7d) verified the presence of lithiated amorphous Li_xSi.[6,41] The peaks at 0.35 and 0.53 V in the anodic sweep of both the electrodes correspond to the delithiation reactions:[5–7]

$$\text{Li}_x\text{Si} \rightarrow \text{a-Si} + x\text{Li}^+ + x\text{e}^- \quad (5)$$

It is worth noting that the area enclosed by the CV curves between 1.5 and 3.0 V of the C–Si/F–CNF electrode was much larger than that of the Si/Fe/CNF electrode. This finding is a reflection of much enhanced Li ion storage capacities by redox reactions[24–26] due to the oxygenated functional groups created by the HNO_3 treatment (Fig. 4).

The electrochemical performance was evaluated using a LAND system between 0 and 3.0 V and the results are shown in Fig. 6. The initial charge/discharge profiles (Fig. 6a), in which discharge refers to the Li–Si alloying process,[4] show that the C–Si/F–CNF electrode presented a remarkable original discharge capacity as high as 2556 mA h g^{-1}, which is 55% higher than the corresponding value of 1650 mA h g^{-1} for the Si/

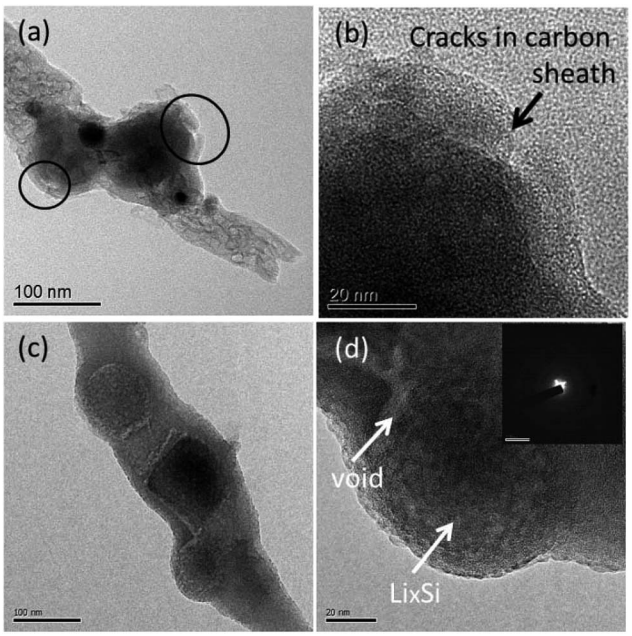

Fig. 7 *Ex situ* TEM images of fully lithiated (a and b) Si/Fe/CNF and (c and d) C–Si/F–CNF composite electrodes after the second cycle.

Fe/CNF electrode. The much higher initial capacity delivered by the former electrode compared with the latter counterpart is attributed to many factors including the following: the removal of the electrochemically inert Fe_3C particles, as proven from Fig. S6;† additional Li ion storage sites arising from the numerous pores and oxygenated functional groups; and the favored SEI layers formed through electrolyte decomposition.[11,25] The initial coulombic efficiency (CE) of the C–Si/F–CNF electrode was lower than the corresponding value of the Si/Fe/CNF electrode, *i.e.* 60.1 *vs.* 81.1%, due to the highly porous structure and functional groups which favoured the irreversible electrochemical process.[42,43] In the following cycles, the CE was fully recovered to ~97% and remained stable. The CEs of the C–Si/F–CNF electrode warrant further discussion. While the average CE was 96.2% for the initial 2–7 cycles (Fig. 6b), the average CE value increased to 98.5% in the following cycles which is comparable or superior to those reported in the literature,[10–22] suggesting excellent cyclic stability. The increased CEs after the 7th cycle can be interpreted by the formation of SEI layers and the stability *via* pre-cycling.[44] The irreversibility of the C–Si/F–CNF electrode with a CE below 100% at 0.5 A g^{-1} can be explained by Li ion trapping in the large active material due to the slow Li release kinetics as well as the gradual formation of SEI layers from the repeatable volume changes of the Si particles.[45] After 40 cycles at 0.5 A g^{-1}, the C–Si/F–CNF electrode maintained a remarkable reversible capacity of ~1300 mA h g^{-1}, which is much higher than the other electrodes, including those containing bare Si, Si/CNF and Si/Fe/CNF composites (Fig. 6b).

The superior electrochemical performance of the C–Si/F–CNF electrode was further demonstrated by cyclic tests at very high current densities of 2.0, 5.0 and 8.0 A g^{-1} (Fig. 6c and S7†) – much more rigorous testing conditions than the most previous reports on similar Si/CNF electrodes.[10–22] Two cycles were initially applied at low current densities before taking the high-rate tests to allow the active Si particles to be ready for reactions.[23,41] The C–Si/F–CNF electrode had initial reversible capacities of 793.6, 623.5 and 519.7 mA h g^{-1} at 2, 5 and 8 A g^{-1}, respectively; and even after 70 cycles they remained at high values of 770, 580 and 422 mA h g^{-1} with remarkable capacity retentions of 97, 93 and 83%, respectively. When these values are compared with major outcomes reported recently of similar electrodes prepared from electrospun Si/CNF or/and functionalized CNF anode materials, the results delivered by the current electrodes are among the best, see Table 2. Nevertheless, it should be noted that the high rate capacities gradually faded after about 70 cycles due to the combination of unfavourable processes, like large volume expansion, electrochemical sintering of Si particles and electrolyte consumption.

Apart from the extremely high cyclic stability at high current densities, the C–Si/F–CNF electrode also exhibited impressive rate performance (Fig. 6d and e). After 60 cycles at different current densities ranging from 0.1 to 4.0 A g^{-1}, the composite

Table 2 Comparison of electrochemical performance between the current C–Si/F–CNF electrode and electrospun CNF electrodes or containing Si particles from the literature

	Electrochemical performance			
Materials & structures	Capacity (mA h g^{-1})	Current (A g^{-1})	Cycle number	Ref.
Void Si/CNT	~850	1	200	10
Si/CNF	700	0.05	30	11
Si/CNF core–shell	590	0.05	50	15
Si/CNT/CNF	911	0.05	45	16
Si/CNF	711	0.05	40	17
Si/porous CNF	1100	0.5	100	18
Si/hollow graphite	500	5	50	22
Functionalized CNF	318	3	70	25
Hollow CNT/CNF	380	5	—	26
C–Si/F–CNF	770	2	70	Current work
	580	5	70	

Table 3 Resistance parameters, R_u, R_{sei} and R_{ct}, obtained from the simulation data in Fig. 6f

Electrodes	R_u/Ω	R_{sei}/Ω	R_{ct}/Ω
Si/CNF	7.4	102.7	201.3
Si/Fe/CNF	7.2	90.8	113.7
C–Si/F–CNF	7.4	71.2	58.7

anode delivered a remarkable reversible capacity of 1178 mA h g^{-1} when the current density was reverted to 0.1 A g^{-1}. The Si/Fe/CNF electrode presented marginally lower capacities than the C–Si/F–CNF electrode depending on current densities, which is attributed to its high electrical conductivity (Table 1) and partially porous structure. The Si/CNF electrode had generally much poorer performance than the other two.

To clarify the improved electrochemical performance of the C–Si/F–CNF electrode, the EIS spectra obtained after rate tests[46–49] along with the equivalent circuit and *Z*-view software simulated results are shown in Fig. 6f and Table 3. The impedance spectra can be explained on the basis of an equivalent circuit with uncompensated resistance (R_u), charge-transfer resistance (R_{ct}) and Warburg impedance (Z_w). The constant-phase elements (CPE1) of the SEI layers and the constant phase elements (CPE2) of the electrode were also taken into account. R_u refers to the electronic and ionic resistances of two electrodes and the interface of electrolyte/separator.[47] The slope line obtained at low frequencies is attributed to Z_w, corresponding to Li ion diffusion in the active materials.[48] According to the simulated resistance parameters in Table 3, the SEI resistances (R_{sei}) and R_{ct} of the C–Si/F–CNF electrode were apparently the lowest among all electrode materials studied, verifying its fast ion/electron transfer due to the highly graphitized and porous structure.

To study the aforementioned effective relief of the volumetric change of Si particles by the nanocavities, *ex situ* TEM images were taken after full lithiation in the 2nd cycle, as shown in Fig. 7. Cracks in the porous carbon sheaths were revealed in the Si/Fe/CNF electrode resulting from the volume expansion of lithiated Si particles (Fig. 7a and b). It is believed that these cracks are detrimental to stable cyclic behavior because the electrolyte would make a direct contact with the fresh Si causing the depletion of the electrolyte, the formation of thick SEI layers and even the degradation of the active materials.[39,40] In sharp contrast, the C–Si/F–CNF electrode maintained the carbon sheaths intact, continuously protecting the active Si particle inside (Fig. 7c and d). Some cavities or voids remained even after full lithiation, indicating the capability to accommodate further stresses. This observation is also consistent with the low Li ion transfer resistance of the electrode sustained after the rate test of 70 cycles (Fig. 6f).

4. Conclusions

In situ N-doped, porous graphitic carbon nanofiber electrodes containing nanocavities surrounding the Si particles were synthesized by facile, one-pot electrospinning followed by electroless etching and acid functionalization. The novel C–Si/F–CNF composite electrodes delivered an exceptionally high initial reversible capacity of 1548 mA h g^{-1} at 0.1 A g^{-1} as well as a remarkable capacity of 1178 mA h g^{-1} when the current density was reverted to 0.1 A g^{-1} after 60 cycles at different current densities. When tested after 70 cycles at high current densities of 2.0 and 5.0 A g^{-1}, the electrode presented reversible capacities as high as 770 and 580 mA h g^{-1}, respectively, both with excellent capacity retention. The comparison with similar electrospun Si/CNF and functionalized CNF anodes clearly indicates superior electrochemical performance of the present work. The above findings can be attributed to unique structural and functional features created in CNFs, including (i) *in situ* N-doping to enhance the electrical conductivity, (ii) highly graphitic structure to facilitate fast electron transport, (iii) porous structure to enhance Li ion transfer, especially during the high-rate test, and (iv) plenty of oxygenated functional groups to provide extra Li ion storage sites. In particular, the nanocavities created around Si particles by electroless etching allowed the encapsulated Si particles to expand freely without destroying the outer carbon sheath. The stress relieving action guaranteed structural integrity and sustained stability of the electrode after long cycles.

Acknowledgements

This project was financially supported by the Research Grants Council of Hong Kong SAR (GRF Projects 613811 and 613612). The authors also appreciate the technical assistance from the Materials Characterization and Preparation Facilities (MCPF) at HKUST.

Notes and references

1 J. M. Tarascon and M. Armand, *Nature*, 2001, **414**, 359.
2 M. Armand and J. M. Tarascon, *Nature*, 2008, **451**, 652.
3 J. R. Szczech and S. Jin, *Energy Environ. Sci.*, 2011, **4**, 56.
4 U. Kasavajjula, C. Wang and A. J. Appleby, *J. Power Sources*, 2007, **163**, 1003.
5 X. Su, Q. Wu, J. Li, X. Xiao, A. Lott, W. Lu, B. W. Sheldon and J. Wu, *Adv. Energy Mater.*, 2014, **4**, 1.
6 M. T. McDowell, S. W. Lee, W. D. Nix and Y. Cui, *Adv. Mater.*, 2013, **25**, 4966.
7 M. L. Terranova, S. Orlanducci, E. Tamburri, V. Guglielmotti and M. Rossi, *J. Power Sources*, 2014, **246**, 167.
8 M. Inagaki, Y. Yang and F. Kang, *Adv. Mater.*, 2012, **24**, 2547.
9 B. Zhang, Y. Yu, Z. Huang, Y. B. He, D. Jang, W. S. Yoon, Y. W. Mai, F. Kang and J. K. Kim, *Energy Environ. Sci.*, 2012, **5**, 9895.
10 H. Wu, G. Zheng, N. Liu, T. J. Carney, Y. Yang and Y. Cui, *Nano Lett.*, 2012, **12**, 904.
11 K. Fu, L. Xue, O. Yildiz, S. Li, H. Lee, Y. Li, G. Xu, L. Zhou, P. D. Bradford and X. Zhang, *Nano Energy*, 2013, **2**, 976.
12 Z. L. Xu, B. Zhang, Z. Q. Zhou, S. Abouali, M. A. Garakani, J. Huang, J. Q. Huang and J. K. Kim, *RSC Adv.*, 2014, **4**, 22359.
13 L. Ji and X. Zhang, *Carbon*, 2009, **47**, 3219–3226.

14 T. H. Hwang, Y. M. Lee, B. S. Kong, J. S. Seo and J. W. Choi, *Nano Lett.*, 2012, **12**, 802.
15 B. S. Lee, S. B. Son, K. M. Park, J. H. Seo, S. H. Lee, I. S. Choi, K. H. Oh and W. R. Yu, *J. Power Sources*, 2012, **206**, 267.
16 B. S. Lee, S. B. Son, J. H. Seo, K. M. Park, G. Lee, S. H. Lee, K. H. Oh, J. P. Ahn and W. R. Yu, *Nanoscale*, 2013, **5**, 4790.
17 L. Ji and X. Zhang, *Energy Environ. Sci.*, 2010, **3**, 124.
18 X. Zhou, L. J. Wan and Y. G. Guo, *Small*, 2013, **9**, 2684.
19 Y. Li, G. Xu, L. Xue, S. Zhang, Y. Yao, Y. Lu, O. Toprakci and X. Zhang, *J. Electrochem. Soc.*, 2013, **160**, A528.
20 Z. L. Xu, B. Zhang and J. K. Kim, *Nano Energy*, 2014, **6**, 27.
21 X. Zhou and Y. G. Guo, *J. Mater. Chem. A*, 2013, **1**, 9019.
22 J. Kong, W. A. Yee, Y. Wei, L. Yang, J. M. Ang, S. L. Phua and X. Lu, *Nanoscale*, 2013, **5**, 2967.
23 B. Wang, X. Li, X. Zhang, B. Luo, Y. Zhang and L. Zhi, *Adv. Mater.*, 2013, **25**, 3560.
24 S. W. Lee, N. Yabuuchi, B. M. Gallant, S. Chen, B. S. Kim, P. T. Hammond and S. H. Yang, *Nat. Nanotechnol.*, 2010, **5**, 531.
25 B. Zhang, Z. L. Xu, Y. B. He, S. Abouali, M. A. Garakani, E. K. Heidari, F. Kang and J. K. Kim, *Nano Energy*, 2014, **4**, 88.
26 Y. Chen, X. Li, K. Park, J. Song, J. Hong, L. M. Zhou, Y. W. Mai, H. T. Huang and J. B. Goodenough, *J. Am. Chem. Soc.*, 2013, **135**, 16280.
27 X. Li, P. Meduri, X. Chen, W. Qi, M. H. Engelhard, W. Xu, F. Ding, J. Xiao, W. Wang, C. Wang, J. G. Zhang and J. Liu, *J. Mater. Chem.*, 2012, **22**, 11014.
28 X. Zhou, J. Tang, J. Yang, J. Xie and L. Ma, *Electrochim. Acta*, 2013, **87**, 663.
29 N. Liu, H. Wu, M. T. McDowell, Y. Yao, C. Wang and Y. Cui, *Nano Lett.*, 2012, **12**, 3315.
30 N. Liu, Z. Lu, J. Zhao, M. T. McDowell, H. W. Lee, W. Zhao and Y. Cui, *Nat. Nanotechnol.*, 2014, **9**, 187.
31 Y. Park, N. S. Choi, S. Park, S. H. Woo, S. Sim, B. Y. Jang, S. M. Oh, S. Park, J. Cho and K. T. Lee, *Adv. Energy Mater.*, 2013, **3**, 206.
32 E. P. Sajitha, V. Prasad, S. V. Subramanyam, S. Eto, K. Takai and T. Enoki, *Carbon*, 2004, **42**, 2815.
33 K. W. Kolasinski, *Curr. Opin. Solid State Mater. Sci.*, 2005, **9**, 73.
34 K. W. Kolasinski, *J. Phys. Chem. C*, 2010, **114**, 22098–22105.
35 L. Oakes, A. Westover, J. W. Mares, S. Chatterjee, W. R. Erwin, R. Bardhan, S. M. Weiss and C. L. Pint, *Sci. Rep.*, 2013, **3**, 3020.
36 Y. Shen and A. C. Lua, *Sci. Rep.*, 2013, **3**, 3037.
37 B. Zhang, Y. Yu, Z. L. Xu, S. Abouali, M. Akbari, Y. B. He, F. Kang and J. K. Kim, *Adv. Energy Mater.*, 2014, **4**, 1301448.
38 C. Morant, J. Andrey, P. Prieto, D. Mendiola, J. M. Sanz and E. Elizalde, *Phys. Status Solidi A*, 2006, **203**, 1069.
39 M. Gu, Y. Li, X. Li, S. Hu, X. Zhang, W. Xu, S. Thevuthasan, D. R. Baer, J. G. Zhang, J. Liu and C. Wang, *ACS Nano*, 2012, **6**, 8439.
40 H. Wu, G. Chan, J. W. Choi, I. Ryu, Y. Yao, M. T. McDowell, S. W. Lee, A. Jackson, Y. Yang, L. Hu and Y. Cui, *Nat. Nanotechnol.*, 2012, **7**, 310.
41 B. Wang, X. Li, X. Zhang, B. Luo, M. Jin, M. Liang, S. A. Dayeh, S. T. Picraux and L. Zhi, *ACS Nano*, 2013, **7**, 1437.
42 Y. S. Hu, P. Adelhelm, B. M. Smarsly, S. Hore, M. Antonietti and J. Maier, *Adv. Funct. Mater.*, 2007, **17**, 1873.
43 M. Ge, J. Rong, X. Fang, A. Zhang, Y. Lu and C. Zhou, *Nano Res.*, 2013, **6**, 174.
44 D. S. Jung, T. H. Hwang, S. B. Park and J. W. Choi, *Nano Lett.*, 2013, **13**, 2092.
45 W. J. Zhang, *J. Power Sources*, 2011, **196**, 13–24.
46 H. Tang, J. Tu, X. Liu, Y. Zhang, S. Huang, W. Li, X. Wang and C. Gu, *J. Mater. Chem. A.*, 2014, **2**, 5834–5840.
47 Y. B. He, M. Liu, Z. L. Xu, B. Zhang, B. Li, F. Kang and J. K. Kim, *Energy Technol.*, 2013, **1**, 668–674.
48 B. Zhang, Y. Yu, Y. Liu, Z. D. Huang, Y. He and J. K. Kim, *Nanoscale*, 2013, **5**, 2100.
49 M. Zhou, T. Cai, F. Pu, H. Chen, Z. Wang, H. Zhang and S. Guan, *ACS Appl. Mater. Interfaces*, 2013, **5**, 3449–3455.